36th AIAA Fluid Dynamics Conference and Exhibit
5 - 8 June 2006, San Francisco, California

AIAA 2006-2866

The Aerodynamics of Compliant Membrane Wings Modeled on Mammalian Flight Mechanics

Ricardo Galvao[*], Emily Israeli[*]. Arnold Song[†], Xiaodong Tian[‡], Kristin Bishop[§],
Sharon Swartz[**] and Kenneth Breuer[††]
Brown University, Providence RI 02912, USA

Mammalian flight is characterized by several features unique and distinct from the flight of both insects and birds. One such feature is the use of thin compliant wings as the lifting surface. Motivated by this, we present experimental results on the aerodynamics of compliant membrane wing models of low aspect ratio, performed at low Reynolds numbers, ranging from 30,000 to 100,000. Lift and Drag coefficients are measured over a range of angles of attack from -5 to 60 degrees. In addition the deformation of the wing due to aerodynamic loading is directly measured using a stereo photogrammetric method. Results indicate that the compliant wings' deformation increases with both angle of attack and that deformation scales with dynamic pressure until the onset of stall at which point inertial scaling fails. Stall on compliant wings occurs at higher angles of attack and is gentler than on a similar wing in which the membrane does not deform. Unsteady membrane vibrations are also measured and characterized.

Nomenclature

C_{ij}	=	lift/drag (i) transformation coefficient for lift/drag load cell pair (j)
C_D	=	drag coefficient
C_L	=	lift coefficient
c	=	chord
Fx	=	drag acting on wing
Fz	=	lift acting on wing
Re	=	Reynolds number
ΔV_x	=	drag load cell pair voltage differential
ΔV_z	=	lift load cell pair voltage differential
x	=	streamwise coordinate
y	=	spanwise coordinate
z	=	altitude coordinate

I. Introduction

Low Reynolds number, low aspect ratio (*LAR*) aerodynamics is an area of increased research activity, driven in large part by the recent interest in micro-sized aircraft design[1, 2] as well as the growth of quantitative studies of flight in insects, birds and bats. *LAR* wings composed of thin and very flexible membranes are unique to flying and gliding mammals, such as bats, flying squirrels and sugar gliders[3, 4] and these animals exhibit extraordinary flight capabilities with respect to maneuvering and agility that are not observed in other species of comparable size. Birds, which are have been studied extensively,[4-6] have relatively rigid wings with limited motion, while insects, which fly at much lower Reynolds numbers, are typically characterized by rigid wings moving with a relatively simply

[*] Undergraduate Student, Division of Engineering
[†] Graduate Student, Division of Engineering
[‡] Research Scientist, Department of Ecology and Evolutionary Biology
[§] Graduate Student, Department of Ecology and Evolutionary Biology
[**] Associate Professor, Department of Ecology and Evolutionary Biology
[††] Professor, Brown University, Division of Engineering, Box D Providence RI 02912, Senior Member, AIAA.

articulated flapping motion[7]. Bats, on the other hand, have an extremely high degree of articulation in the wing (the elbow, wrist and finger joints). More relevant to the current investigation is the fact that the wing surface in bats and other flying mammals is unusual in that it is composed of a thin wing consisting of a highly anisotropic, compliant skin membrane (Fig. 1). This observation suggests that a potentially useful feature for engineered maneuverable micro flight vehicles might be the incorporation of flexible wing membranes as lifting surfaces.

Figure 1. Examples of mammalian flight. *The sugar glider on the left can perform controlled glides at high angles of attack over distances of 100 meters. The unique wing morphology of bats (right) include their skeletal structure and thin wing membranes.*

An additional feature (and complication) of mammalian flight is the fact that they operate in a highly unsteady fashion and at an intermediate Reynolds number regime where many complex aerodynamic phenomena, such as transition to turbulence and laminar separation, are both present and hard to predict. Although this area of aerodynamics has not been studied extensively, there are some notable exceptions in recent years[2, 8, 9]. These studies have investigated *LAR* wings and airfoils at low Reynolds numbers in an attempt to better understand the aerodynamic performance of MAVs.

As an example of an initial inquiry to understand MAV aerodynamics, Shyy and coworkers[8] used a computational analysis of 'low Reynolds airfoils' to ascertain the effect of thickness and camber, as well as generating pressure surface profiles. Well-known airfoils: the *NACA0012* and *CLARK-Y* were investigated, and compared with the performance of specially designed low-Re wing sections over a range of *Re* (~7.5 x 10^4 to 2.0 x 10^6) and angles of attack. The low-Reynolds airfoils are characterized by highly cambered profiles, low area, and sharply angled leading and trailing edges (the *UF* airfoil is also quite a bit thinner than the other airfoils in the assessment). The authors concluded that increased camber and reduced thickness airfoils have more favorable lift-to-drag ratio as *Re* number decreases, while the conventional airfoils, i.e. *NACA0012* and *CLARK-Y*, were found to be less suited to the low-*Re* regime associated with MAVs.

On the experimental front, recent studies by Mueller and coworkers have specifically examined *LAR* thin/flat/cambered-plate wings[10] and several planforms of *LAR* wings[9] over a range of Reynolds numbers, *Re* = 70,000 to 200,000. Both studies explore the behavior of aerodynamic force coefficients, mainly lift and drag, as well as range efficiency (lift-to-drag ratio) and power efficiency ($C_L^{3/2}/C_D$) with respect to aspect ratio and *Re* dependence. Torres and coworkers suggest that the large non-linearities in the lift curves for wings with aspect ratios less than 1.25 are due to wing tip vortices. These flow structures contribute to an increased maximum lift, C_{Lmax}, and the delay of stall to a larger angle of attack. The interaction of the wingtip vortices with the flow over the lifting surface for *LAR* wings is analogous to the delta wing, which has vortex lift at high angles of attack.

A strong thrust in the recent research on MAVs focuses on designs that employ membrane wings that have variable-camber or an adaptive-wing structure[1, 2]. This is desirable for several reasons, and yet a detailed analysis of the complexities that compliance adds to the aerodynamic characteristics of a flexible membrane wing does not appear to be been fully pursued. One motivation for the utilization of flexible membrane wings is to mimic the aeromechanics of natural flyers such as bats because MAVs operate in a similar flight parameter space as these biological flight systems, i.e. flying at low *Re* with *LAR* wings. As the evolution of MAV design progresses, little basic science research has attempted to develop a model of the interplay of aerodynamic contributing to the better performance of flexible membrane flyers. The adaptive nature of the membrane wing may give MAVs the potential to mimic the extraordinary flight agility of bats. The morphing capability of the wing structure is the product of the interaction between fluid and structural capabilities. Recently, Shyy[2] has reviewed the recent computational and experimental work relating to MAV research. He also discusses the development of computational techniques to assess the flow structure associated with *LAR*, low Reynolds wings and the generation of optimization techniques for MAV wing shape. The structural deformation or dynamics of the flexible membrane greatly contributes to the aerodynamic forces over the wing and the wing performance. Clearly, in looking to nature's flyers as inspiration, MAV designers have recognized the potential of flexible membrane wings to achieve improved agility and efficiency.

The study of the full complexity of mammalian flight is challenging but is nevertheless underway[3, 11]. However, a significant challenge in working with live animals (and something that is somewhat unfamiliar to the traditional aerodynamics community), is the requirement that the testing must be accomplished in a safe and humane manner, and furthermore, that it is difficult, if not impossible, to isolate unique contributions that different characteristics of an animal's morphology contribute to its overall aerodynamic performance. To address these issues, we have thus embarked on a systematic study with an attempt to isolate different morphological features present in mammalian flight, and to explore the role that each plays. The current study focuses on the effects of thin membrane wings on aerodynamic performance and the present manuscript, which is the first step in this direction, has two goals: firstly to characterize the aerodynamic performance of compliant membrane wings and secondly to explore the dynamics of the membrane as it is subjected to aerodynamic loads. To accomplish this, we describe the design, fabrication and testing of simple "canonical" membrane wings with low aspect ratio. The wing is tested in a low-speed wind tunnel over a range of (low) Reynolds numbers and angles of attack. Both lift and drag forces are measured for four wing configurations. In a separate but overlapping series of experiments, we have measured the three-dimensional shape of the wing as it deforms while subject to aerodynamic loading. This is accomplished using high-speed, stereo photogrammetry which allows us to measure not only the static deflection of the wing but also the onset of unsteady wing motions.

II. Experimental Procedure

All experiments were conducted in the low-speed, low-turbulence wind tunnel at Brown University. The wind tunnel is a closed-return facility in which free stream velocities are controlled by a constant speed variable angle axial fan. The test section measures 61.0 cm by 61.0 cm.

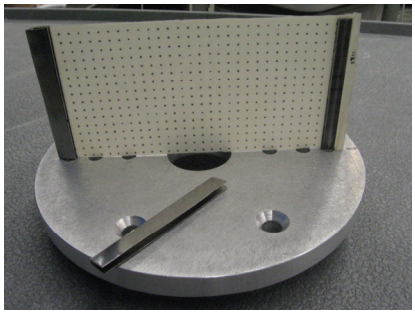

Figure 2. Photograph of the flexible wing model. *The trailing edge spring clamp has been removed for clarity. The dot array is tracked by the photogrammetry system.*

A. Flexible wing models

A compliant membrane wing was designed and manufactured for the experiments. The rectangular wing is composed of a compliant latex membrane held between two stainless steel posts located at the leading and trailing edges (Fig. 2). The posts measure 6.0 cm in height and are secured to an aluminum mounting plate designed to attach to the force balance which is mounted on the test section ceiling. At either end of wing, the membrane material is inserted through a slit aligned with the centerline of the post then secured using spring steel clamps. With the clamps in place, the leading and trailing edges are approximately parabolic in shape with a maximum thickness of 3.7 mm. The fully assembled wing measures 12.9 cm (chord, *c*) by 5.9 cm (half-span, *b*), giving a half-wing aspect ratio of 0.46. We should note that the assembly technique did not carefully control the tension in the wing membrane, only adjusting it so that it seemed taut, but not stretched, in its default position (in absence of aerodynamic forces). As a result, direct comparisons between wings of different membrane materials are taken to be merely qualitative, since the results will depend, not only on the wing membrane material, but also on the pre- tension of the wing with no aerodynamic loading.

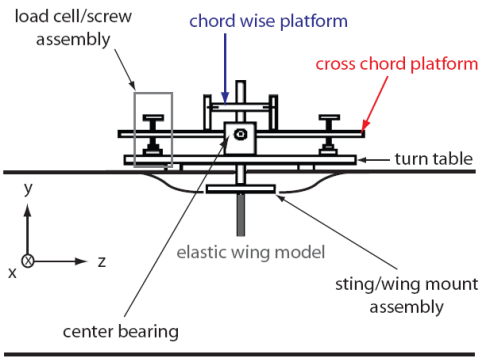

Figure 3. Schematic of the wind tunnel configuration. *The wing hangs down into the test section, mounted on a two-axis gimbal. Lift and drag are measured from the output of four load cells, each attached to an orthogonal axis of the force balance*

B. Lift and Drag Measurements

The wing is mounted upside down on a gimbaled, two-axis force balance for measurement of lift and drag (Fig. 3). The platforms are aligned to be orthogonal so as to decouple the two horizontal components of the aerodynamic forces, each of which is measured using a pair of load cells. The entire force balance assembly is mounted to a turntable which allows

adjustment of the angle of attack. The orientation of the orthogonal force platforms is fixed with respect to the chord line of the wing as the angle of attack is varied. The load cells are pre-loaded so that, as the aerodynamic force increases, the output of one load cell increases while the output of the other decreases. Thus, the applied load is determined from the difference between the two load cell readings, an arrangement that minimizes common-mode noise due to the vibrations of the apparatus. Voltages were acquired using a 16-bit A/D system sampling at 4 kHz and averaging over 50 seconds. Although this can ultimately allow unsteady force measurements, this was not attempted in the current series of experiments.

The force balance measures the applied moment about a center bearing. Assuming that the lines of action of the aerodynamic forces intersect the mid-span of the wing, we can then recover the lift and drag acting on the wing. The wing deflection measurements presented later in this paper support the validity of this assumption. However, planned improvements to force balance apparatus will allow future experiments to simultaneously measure the aerodynamic forces and the center of pressure.

At any given speed and angle of attack, the forces in the chordwise and cross-chord directions may be found from a linear combination of the four load cell voltages. Nominally, two load cells will contribute equal and oppositely to each component of force. However, each load cell has slightly different gain, and a slight misalignment between the axes of the force balance and the axis of the wing is unavoidable. For this reason we utilize the voltage differentials, ΔV_x and ΔV_z, of *both* load cell pairs in the determination of both F_x (drag) and F_z (lift). This can be expressed in matrix form:

$$\begin{bmatrix} C_{xx} & C_{xz} \\ C_{zx} & C_{zz} \end{bmatrix} \begin{bmatrix} \Delta V_x \\ \Delta V_z \end{bmatrix} = \begin{bmatrix} F_x \\ F_z \end{bmatrix} \tag{1}$$

The coefficient matrix is determined from a series of measurements performed by applying static forces in both the streamwise and spanwise directions. For calibration, the applied forces in the lift and drag coordinate directions ranged from 0.98 to 4.95 N. These calibration measurements were then converted to a series of linear weights using a generalized linear regression based on a singular value decomposition (SVD) of the over-constrained linear system:

$$\begin{bmatrix} \Delta V_{x,1} & \Delta V_{z,1} & 0 & 0 \\ \vdots & \vdots & \vdots & \vdots \\ \Delta V_{x,i} & \Delta V_{z,i} & 0 & 0 \\ 0 & 0 & \Delta V_{x,1} & \Delta V_{z,1} \\ \vdots & \vdots & \vdots & \vdots \\ 0 & 0 & \Delta V_{x,i} & \Delta V_{z,i} \end{bmatrix} \begin{bmatrix} C_{xx} \\ C_{xz} \\ C_{zx} \\ C_{zz} \end{bmatrix} = \begin{bmatrix} F_{x,1} \\ \vdots \\ F_{x,i} \\ F_{z,1} \\ \vdots \\ F_{z,i} \end{bmatrix}, \; i = 1, \ldots, N \tag{2}$$

where the number of calibration measurements is denoted by N. However, we can decompose the matrix of measured voltages, denoted here as **A,** via SVD

$$\mathbf{A} = \mathbf{U}\mathbf{S}\mathbf{V}^T .$$

Let the dimension of voltage matrix, **A**, be of dimension m x n. We define **S** to be a m x n diagonal matrix of the singular values of the original matrix **A**. **U** and **V** are then defined to be matrices of dimensions m x m and n x n, respectively, which have orthogonal columns so that

$$\begin{aligned} \mathbf{U}^T\mathbf{U} &= \mathbf{I} \\ \mathbf{V}^T\mathbf{V} &= \mathbf{I} \end{aligned} \tag{3}$$

We can write Eq. (2) as

$$\mathbf{A}\mathbf{c} = \mathbf{f} \tag{4}$$

where **c** and **f** are the vectors containing the transformation coefficients and applied forces respectively. Solving for **c**,

$$\mathbf{c} = \mathbf{A}^{-1}\mathbf{f} = \mathbf{V}\mathbf{S}^{-1}\mathbf{U}^T\mathbf{f} . \tag{5}$$

Because the inverse of **S** is used to determine **c**, artificially large coefficient values may result from the very small entries of **S**, i.e. singular values of negligible importance. Therefore, we employ a threshold for which the spuriously large values of the entries of $\mathbf{S}^{-1}$ are set to zero.

The calibration was found to be accurate to within 0.9% above a load of 1 N, and no worse than 1.4% over all calibration loads.

C. Wing Deflection Measurements

A stereo photogrammetry system was developed to measure the instantaneous deflection of the wing. Two high speed, complementary metal-oxide semiconductor (CMOS) cameras (IDT X-stream and Photron PCI-1024) were placed outside the wind tunnel test section with an approximate 70° angle of separation between their respective optical axes. For higher angles of attack (above 25°) the camera separation angle was reduced to 60° and the cameras moved closer to one another to be able to maintain the ability to discern markers across the wing membrane at these high angles. The cameras have approximately 1000 x 1000 pixel resolution, which in conjunction with the imaging optics (Nikon 60 mm Micro Nikkor lenses) provided spatial resolution of 0.20 mm per pixel. For this series of experiments, the unsteady motion of the membrane was recorded for 0.5 seconds at 500 Hz (250 frames) at each speed and angle of attack.

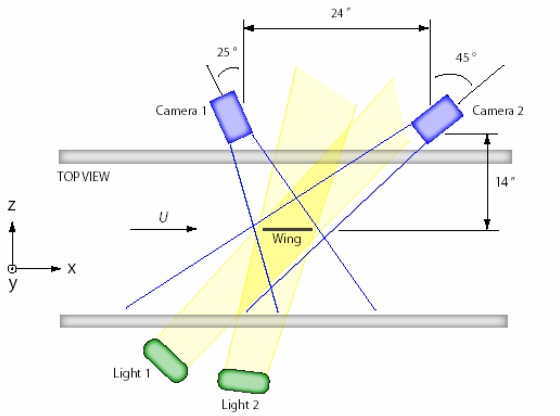

Figure 4. Schematic of photogrammetry system. *The separation angle of the optical axes of the two cameras allow for the reconstruction of a 3-dimensional space from 2-dimensional images via the DLT method.*

Custom software, utilizing direct linear transformation (DLT)[12], was used to recover the coordinates of each marker location in the 3D object space from two 2D images at each time step. A calibration cube consisting of a three-dimensional grid of markers was used to generate the calibration coefficients needed to reconstruct coordinates in the object space via DLT. The dimensions of the cube are 15.2 cm x 7.6 cm x 15.2 cm to ensure that the calibration includes the swept volume of the wing as it is rotated through a range of angles of attack.

Tests were conducted in order to determine the measurement uncertainty in the photogrammetry technique. For these tests, an individual marker was placed at several known distances from a reference location. These coordinates could be resolved with ±25 μm precision. Subsequently, the coordinates of the test marker determined via DLT was compared with the known location. The measurement uncertainty of displacement measurements using the DLT method is less than ±35 μm for in plane displacements and ±40 μm for out of plane displacements, with the reference plane taken to be the plane coincident with the undeflected geometry of the membrane.

D. Testing Procedures

The experiments were conducted in two parts. Lift and drag measurements were acquired over a range of angles of attack (-5 to 60 degrees) and at four different speeds (7 to 20 m/s) corresponding to a Reynolds number range of 70,000 to 200,000. Due to complications arising from the original design of the force balance (which did not affect accuracy, only the ease of experimentation), the experiment initially required turning the wind tunnel off before changing the angle of attack. For this reason, it was not possible to exactly match the velocities at each angle and so the results are presented for a narrow range of Reynolds numbers. Four wing models were tested: a thin non-compliant wing composed of a sheet of 0.50 mm thick steel shim stock (denoted RW02), two compliant membrane wings using latex rubber sheets of thicknesses 0.25 mm and 0.15 mm (denoted EW01 and EW006, respectively), and lastly, a latex membrane wing (0.25 mm thick) in which the membrane was deliberately given 6% slack (denoted EW01s). A second series of experiments was conducted to measure the wing deflection. For these experiments, the velocity was varied from 3 to 12 m/s, and angles of attack varied from -10 to 50 degrees. In this series only the EW01 and EW006 wings were tested. We emphasize, however, that the tension in the compliant wings was not carefully controlled and that as a consequence, comparisons between the EW01 and EW006 results are solely qualitative.

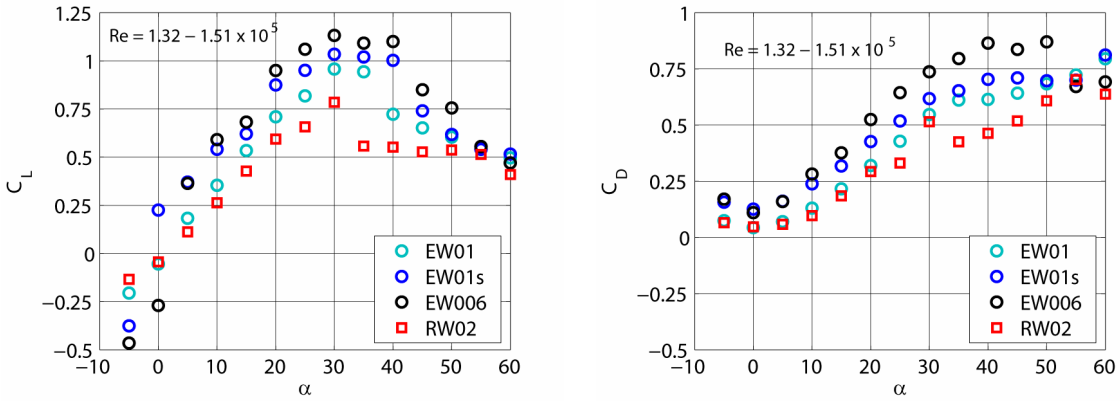

Figure 5. Lift and Drag coefficients. *The aerodynamic force coefficients are shown for four wings: a rigid steel plate (RW02), thin and thick latex membranes (EW006, EW01) and a latex membrane with 6% slack (EW01s).*

III. Results and Discussion

A. Static Wing Performance

An analysis of the time-averaged aerodynamic forces and the consequent membrane deflections characterize the compliant wing's steady performance. We have focused our analysis on the lift and drag curves, in particular the lift slope and behavior in the vicinity of stall, lift-to-drag ratios, and static wing geometry, to further understand the role of compliance in the aerodynamic characteristics of flexible membrane wings. As Fig. 5 demonstrates, the lift slopes of the compliant wings, *EW01* and *EW006*, are greater than that of the rigid model, *RW02*, indicating that the compliance of the wing material substantially improves the lift performance. The degree to which the compliant wings camber is seen to be a monotonically increasing function of angle of attack for small angles, i.e. $\alpha < 30^{\circ}$ (Fig. 6). Because the increase in lift at a fixed angle is roughly proportional to the increase in camber, the variable camber of the compliant wings effectively increases the lift slope. A comparison of the lift slopes of the two compliant wings and the rigid wing demonstrates this point (Table 1), where the thinner membrane, *EW006*, has a larger lift slope than *EW01* which in turn has a higher lift slope than the non-compliant, or rigid, wing. Photogrammetric measurements of the membrane deflection show that, at a fixed angle of attack, the thinner membrane stretches to a greater degree as compared to the thicker membrane, and thus has a greater camber at corresponding angles of attack (Fig. 6).

Model	$dC_L/d\alpha$	% increase
RW01	**0.027/deg**	**--**
EW01	**0.034/deg**	**26**
EW006	**0.047/deg**	**75**

Table 1. Comparison of lift slopes. *The increase in lift slope scales with the compliance of the wing.*

In addition to the magnitude of the lift slope, its derivative in the range of angles of attack near stall is of particular interest, i.e. the severity of the decrease of lift after the onset of stall. The critical angle of attack for the onset of stall is defined for this analysis as the first angle of attack where $dC_L/d\alpha$ becomes zero. It can be seen in Fig. 5 that the severity of the decrease in lift as a result of stall for the rigid wing is attenuated in the compliant membrane wings. Stall occurs due to separated flow on the upper surface of the wing, and is characterized by an increase in the pressure on the upper surface leading to a loss in lift. However, the compliant wings appear to have a natural flow control mechanism which alleviates this affect. At high angles, the camber of the wing is observed to decrease (Fig 5). This appears to be due to the onset of stall, but the de-cambering acts to decrease the severity of the separation, thus delaying the sharp drop in lift force. Thus, the change in the wing's geometry appears to be a an indicator of the flow conditions that may eventually lead to stall. The passive adjustment of camber in the vicinity of stall allows the wing to sustain a significant amount of lift at high angles of attack. Future experiments incorporating time-resolved PIV measurements of the flow field over the compliant wings should provide more details of this fluid-structure interaction.

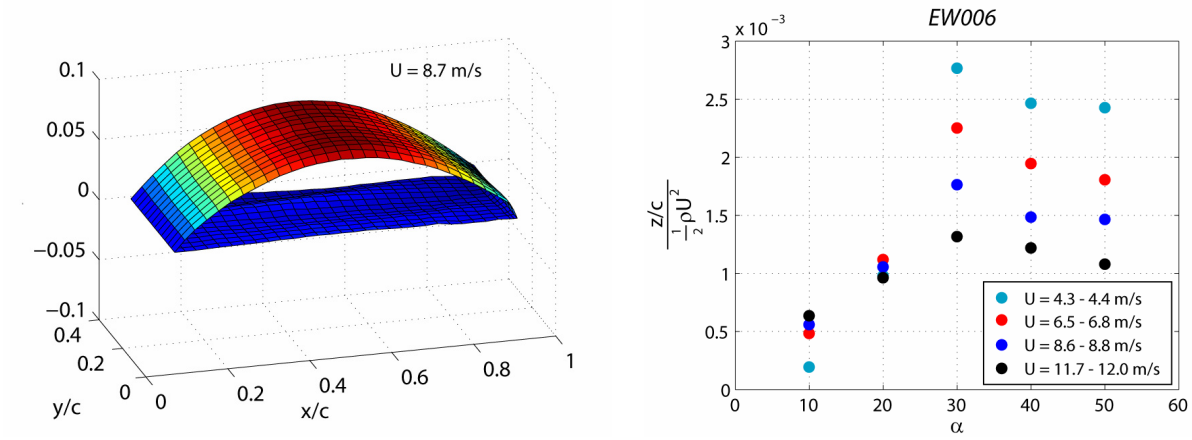

Figure 6. Static deflections of the membrane wing (*EW006*). *A sample deflection of the compliant wing is shown on the left. Note the two-dimensional deflection, and the maximum deflection close to the mid-chord. The maximum deflections are summarized on the right, showing increasing deflection with increasing angle of attack up to the onset of stall. At low angles, the deflection appears to scale with dynamic pressure, although this no longer holds after stall.*

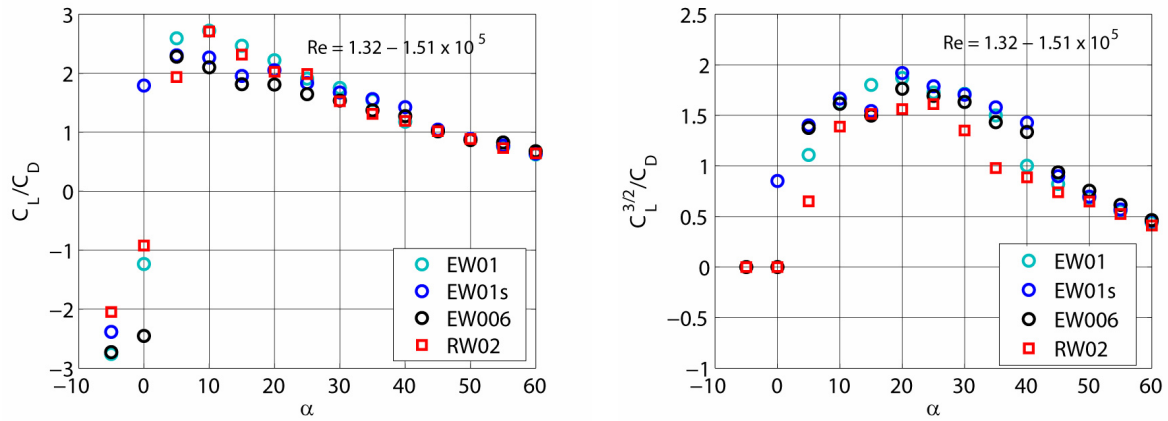

Figure 7. Aerodynamic coefficient ratios. *The aerodynamic force coefficients ratios are shown for four wings: a rigid steel plate (RW02), thin and thick latex membranes (EW006, EW01) and a latex membrane with 6% slack (EW01s).*

This compliance-related lift advantage is evident when one directly compares the lift coefficient curve of the rigid model, *RW02*, to the compliant model, *EW01*. Both wings have a classical "thin-airfoil" stall profile that is characterized by flow separation at the leading edge of the wing with turbulent reattachment further down the wing chord that moves progressively towards the trailing edge as angle of attack increases. This type of stall is generally associated with a softer profile characterized by a gradual bending of the lift curve at maximum lift. Both the rigid and compliant wings are "aerodynamically thin," as a membrane or flat sheet of metal, and are expected to have softer "thin-airfoil" stall. Nevertheless, the compliant wing is able to sustain superior lift at stall with a more gradual curvature at maximum lift as a result of the previously mentioned de-cambering phenomenon. Thus, the compliant wing's even smoother stall is clearly a result of compliance-yielding camber variability. This result relates to mammalian flight since animals can optimize the conformation of their wing to increase aerodynamic performance. The wing models are primitive examples of slight aerodynamic shape/camber optimization and adaptive behavior to sustain lift. Thus, if the wing starts to stall, the top surface pressure rises and the wing de-cambers automatically (at least in a steady sense) to lessen the severity of the pressure increase, producing both a smoother stall profile and delaying stall by 2°-8°.

Figure 5 not only demonstrates the smoother lift decay, but also demonstrates the improvement in lift performance of the compliant wings with respect to the rigid or non-compliant wing. For all *Re* tested, the compliant wing models generate more lift at high angles of attack (25° to 55°) than the rigid wing model. At stall, an

evaluation of C_{Lmax} shows the compliant wing has enhanced lift performance compared to the rigid wing model. The C_{Lmax} quantities reveal an amplification of C_{Lmax} from ~0.79 for the rigid wing to ~0.9-1.13 depending on the compliant wing model.

Offseting the compliant wings' superior static lift performance, the magnitude of their drag is also heightened (Fig. 5). We suggest two reasons for this amplification of drag. First, the higher degree of camber in the compliant wings generates more drag, especially around stall. Second, as will be seen in the subsequent section of this paper, the membrane has aeroelastic instabilities that result in membrane fluctuation and vibration. This instability of the compliant membrane is also a possible factor in the heightened drag of the compliant wing. It is noted that the slack and most compliant wing (*EW01s* and *EW006*) have the highest drag. These wings have greater camber capability and more susceptibility to membrane unsteadiness consistent with the suggested hypothetical mechanism for greater drag generation.

To conclude our discussion on the compliant wing's static aerodynamic performance, we comment on the aerodynamic coefficient ratios vs. angle of attack profiles associated with each wing (Fig. 7). Flight range efficiency (C_L/C_D) and power efficiency ($C_L^{3/2}/C_D$) are of particular interest for this paper. Both the compliant and stiff wings have similar range efficiencies over all angles of attack characterized by a sustained lift-to-drag ratio over a wide range of angles of attack, particularly post-stall. Thus, both wings sacrifice a high maximum efficiency for improved or optimal efficiency over a range of angles of attack. On the other hand, the power efficiency reflects the aerodynamic superiority of the compliant wing. At high angles of attack (particularly at $\alpha = 35^o$-40^o) the compliant wing attains significantly higher power efficiency values than the rigid wing. This result is expected due to the previously described lift enhancement feature of compliance because the power efficiency parameter emphasizes lift.

The advantageous power efficiency indicates that the superior flight energetics and maneuverability of bat flight is likely a result of the compliant membrane wing. A compliant membrane improves lift performance over a range of angles of attack while maintaining a reasonable level of aerodynamic efficiency conferring a substantial benefit to natural flyers such as bats.

B. Unsteady Membrane Motion

An analysis of the unsteady membrane motion provides a further understanding of several aspects of the compliant wings' aerodynamic behavior. This unsteadiness was apparent during experimentation through noticeable flapping and fluttering of the wing membrane. These fluctuations are quantified by time traces of points on the membrane which show a periodic motion in the z-direction. The strength and nature of these vibrations can be expected to vary with angle of attack and speed. Increasing the angle of attack ultimately leads to leading edge vortex shedding and Reynolds number affects flow attachment as well as the transition to turbulence. The data collected allow for a time-dependent, unsteady analysis of markers on the wing membrane for a range of angles of attack and speed.

The regions of strongest instability of the membrane shape were identified by computing the root-mean-square (rms)

$$z_{rms(i,j)} = \sqrt{\frac{1}{N}\sum_{f=1}^{N}(z_{(i,j)} - \bar{z}_{(i,j)})^2}$$

of the wing membrane fluctuations of each position on the wing, where $z_{i,j}$ is the deflection of the wing at each marker location, $\bar{z}_{i,j}$ is the time-average of the deflection, and N is the number of samples in time (250 in these experiments). The resulting rms value provides a characterization of the intensity of the membrane's oscillation, with a higher rms value corresponding to a larger amplitude motion. The dependence of the maximum rms (maximum over the entire wing) as a function of angle of attack and speed is shown in Fig. 8. At low angles of attack, the rms is quite small with variations of approximately 0.1% of the chord; this is close to but above the spatial resolution of the detection system. However, as the angle of attack increases, the rms of the fluctuations increases, reaching a peak between 20-30 degrees before falling again. Note also that, with some notable exceptions, to be discussed in more detail below, the fluctuations appear to be independent of speed.

The spatial structure of the fluctuations changes at each particular speed and angle of attack sometimes embodying uniform motion, and in other cases the fluctuations are more chaotic. For several cases, a fluid-structure resonance was observed, in which the wing was seen to vibrate in a very well-defined standing wave assumed to be pumped by the vortex shedding from the leading edge. A clear example of this is shown in Fig. 9, which exhibits a standing wave structure with four peaks (three interior nodes). The amplitudes of the node and antinodes as a function of time are also plotted in Fig. 9, clearly showing the harmonic nature of the motion. The significance of the standing wave formation is that wing membrane excitation (one assumes, due to the vortex shedding from the leading edge as the wing approaches stall) coincides with one of the natural harmonic frequencies of the wing membrane. These frequencies are determined by properties such as length and tension of the medium through which the wave is traveling. A Welch power spectral density of the membrane oscillation indicates that the shedding frequency causing the membrane behavior depicted in Fig. 9 is approximately 102 Hz ($St = fc/U = 1.54$).

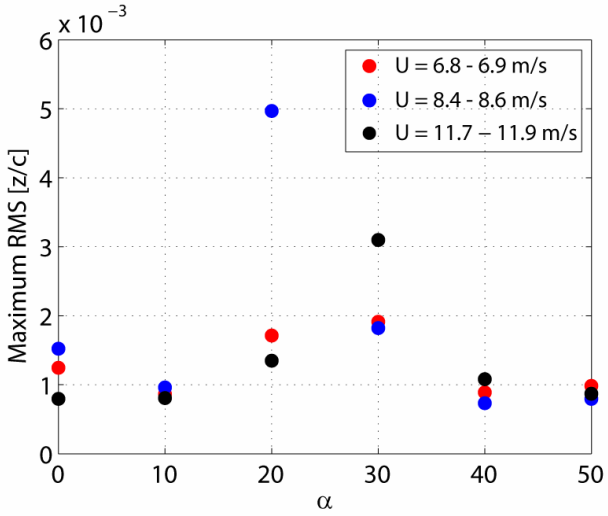

Figure 8. Growth of unsteady membrane motion. *The membrane vibrations (EW01) are observed to grow to a maximum at the point of stall after which they decay. An exception to this is the peak at 20 degrees for the 8.53 m/s speed. This appears to be a resonant condition (perhaps one of many that may exist).*

Another approach in the examination of Reynolds number effect on the wing membrane oscillation is to perform a power spectral density analysis. In the case depicted in Fig. 8, only one distinct frequency peak is noted. However, for other flow speeds at the same angle of attack, multiple peaks are evident. These multiple peaks indicate that a complex flow structure is involved in forcing the membrane vibration. A single frequency disturbance of the membrane may be the result of a simple case of steady shedding of vortices from the leading edge. However, for cases where multiple frequencies are observed, the vortex shedding may have some periodic behavior with a variable shedding frequency, suggesting that the flow over the wing may be in a transition regime or is subject to 3-dimensional effects. In addition, the multiple frequencies observed at particular wind speeds may be the result of interactions between waves reflected off the trailing edge which are no longer at the same frequency as the incident waves generated by the flow. This speed-frequency relation is a result of the flow sweeping vortices across the membrane at a faster rate, thus resulting in a higher frequency of the membrane motion. Frequencies reach a

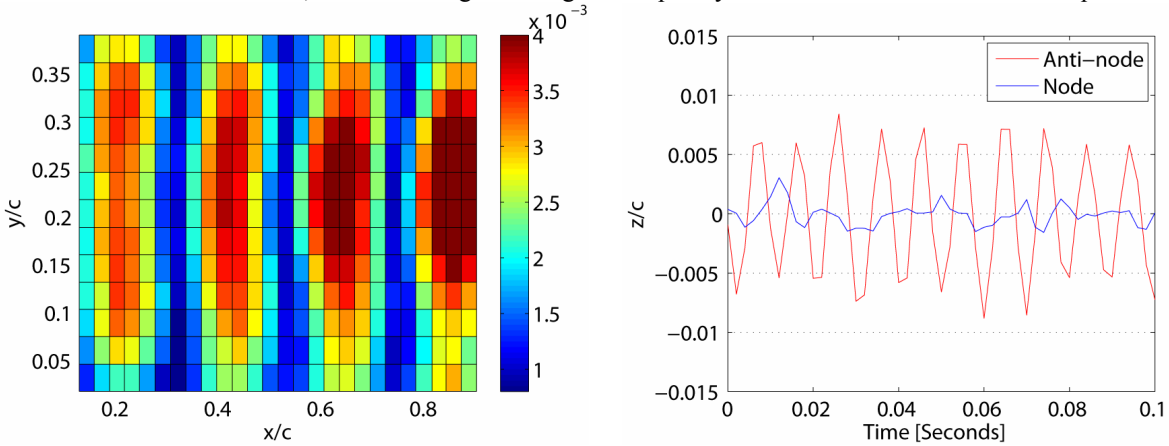

Figure 9. Spatial and temporal structure of the membrane oscillations. *For this example, the wing is vibrating at its 4th structural mode with a clearly defined standing wave established over the wing surface. The temporal behavior of the node and anti-node are shown on the right. The frequency at this condition is approximately 102 Hz. (St = 1.54).*

magnitude of 154 Hz and 176 Hz for *EW006* and *EW01*, respectively, with the maximum frequency in both cases occurring at $\alpha = 30^o$, in the vicinity of the onset of stall.

To isolate the effect of speed on the unsteady deflection of the compliant wing, an angle of attack was chosen from the data for *EW01*. The rms distributions for this wing at $\alpha = 20° \pm 1°$ are compared at four speeds, corresponding to Reynolds numbers from 3.4×10^4 to 1.1×10^5. It was observed that the development of distinctive regions of high rms oscillations is clearly speed dependent. The formation of interspersed low and high rms regions was not always seen. A true standing wave in which such behavior would be seen only occurs at the resonant and harmonic frequencies of a system. Even a slight divergence from any of these frequencies leads to a wave that is not entirely stationary in the vibrating medium. The resultant wave manifests itself through less distinct or smeared bands of high intensity rms anti-nodes along with less defined nodal regions. The occurrence and behavioral mode of the standing wave has a dependence on wind speed. For the lowest speed, a 2nd harmonic standing wave appears to form. At the two intermediate speeds, we observed more distinct patterns of 3rd and 4th harmonic waves for the lower and higher speed, respectively. For the highest speed a 4th or 5th harmonic oscillation is present, although it should be noted that the fluctuation data is also noisier for these cases. In general, it is seen that the harmonic order of the wave formation is an increasing function of the speed. A finer sweep of Reynolds numbers would be necessary to capture the exact condition at which this standing wave mode occurs in the membrane. Analysis of the coupled membrane-fluid dynamics will be difficult, but a few observations are possible. As the speed increases, not only does the vortex shedding increase, but the membrane camber increases, accompanied by an increase in the membrane tension and hence the frequency of the natural vibration mode (the "drum" mode). Thus, even at fixed angle, the coupled problem has a wealth of subtlety that needs to be explored before the system is fully understood.

By fixing the speed, membrane behavior was analyzed as a function of angle of attack which is the primary driving force of leading edge vortex shedding. Thus, an analysis of the unsteady membrane behavior across multiple angles of attack provides insight into the effect of this phenomenon on the membrane. At angles of attack below 20°, the vibrations of the membrane are relatively chaotic, i.e. there are no well-defined patches or regions of the membrane which oscillate at similar strength. Also, the higher strength oscillations appear to be confined to a band of angles of attack, $20^\circ < \alpha < 30^\circ$, while oscillations of lower strength occur for angles outside of this range, as seen in figure 8. At lower angles, flow is more attached which may serve to dampen membrane vibrations. Thus, any oscillations generated are a result of sporadic fluctuations in the flow and are relatively weak. As vortex shedding becomes more significant leading up to stall, standing waves begin to appear and generate higher intensity membrane oscillations. However, beyond $\alpha = 30°$, the flow becomes detached and does not force the membrane surface in a periodic or concentrated manner. As a result, the post-stall case exhibits a loss of the multiple harmonic standing wave behavior seen leading up to stall and is instead characterized by single band of lower magnitude rms amplitudes. Furthermore, the rms behavior is mirrored by the frequencies of the membrane oscillations. Highest frequencies are observed around stall and then drop to lower values post-stall.

A conceptual "phase map" of the harmonic oscillations using the previously discussed data is shown in Fig. 10. This contour map is an overview of this paper's conclusions on wing membrane motion. The figure summarizes the overall membrane behavior with regard to the observed harmonics over the experimental range of angle of attack and speed. The strength of the membrane vibrations is indicated by the size of the white dot at each measurement station. Finer increments in these parameters will be necessary to more accurately determine transitions from one harmonic to another. Nevertheless, it is shown for *EW006* that 3rd and 4th harmonic oscillation behavior occurs at the speeds studied. Also, for this wing, rms magnitude is larger at these higher speeds for angles of attack close to 30^o. In contrast, the thicker membrane wing *EW01* attains higher harmonics at lower speeds and larger rms magnitudes are seen around 20^o. Concentrated regions of higher rms coincide with the conditions where the most distinct standing wave patterns are observed across the wing membrane. Thus, the locations of these concentrated areas can be altered because they are related to conditions where the flow induced membrane instabilities match the wing's resonant frequency and corresponding harmonics. These characteristic frequencies of the membrane can be easily adjusted by changing the thickness and tension of the compliant membrane. If there are aerodynamic advantages or disadvantages to being in this region, wing characteristics may be altered to locate this area in the appropriate Reynolds number and angle of attack ranges. The ability of flying mammals, such as bats and flying squirrels, to alter the tension of their wing membranes may be a means of optimizing flight performance by modifying the membrane instabilities (both mode and rms amplitude) occurring on their wing.

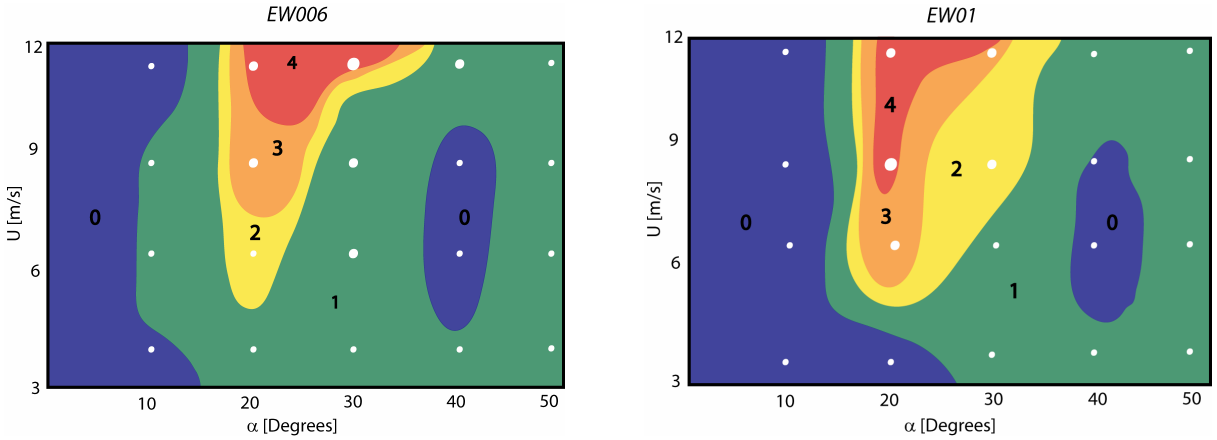

Figure 10. Phase map of membrane fluctuations. *A qualitative map of the wing oscillations are shown as a function of angle of attack and Reynolds number (speed). The white dots mark the locations where measurements were made, and the size of the dot indicates the amplitude of the unsteadiness. At a = 20, higher structural harmonics appear to be excited with increasing speed, although there may be other such resonances at angles and speeds not tested in this series of experiments.*

IV. Conclusions

The data presented here represent the first and still somewhat preliminary attempts to systematically characterize the effects of wing compliance on its static and dynamic aerodynamic performance. These experiments were motivated by mammalian flight observations, but clearly the models tested are quite far removed from biological flight mechanics and at this stage only serve to indicate what kind of aerodynamic phenomena we might expect due to wing membrane compliance. From a purely aeromechanical perspective, however, the system is rich with phenomena that call for further investigation. The static behavior illustrates high lift slopes due to adaptive cambering in response to the aerodynamic loads. Furthermore, the onset of stall is significantly ameliorated by the de-cambering of the wing as the pressure on the upper surface rises due to incipient separation. This effect delays stall and, when it does occur, softens its impact significantly. The cost of this delayed stall is a rise in drag, although not sufficiently serious that range or power ratios are adversely affected.

The unsteady behavior of the wing is also of great interest. Here we see the rise of wing membrane oscillations forced, apparently, by leading edge vortex shedding and at some discrete velocities, a resonance between the two leading to large wing membrane vibrations. Although it is unlikely that animals operate in this regime -- they have intrinsic muscles that can adjust the wing tension so as to avoid such instabilities -- the phenomenon is nevertheless an important one and deserving of further study.

Acknowledgments

We gratefully acknowledge the assistance of the entire Turbulence and Animal Flight Research Lab at Brown, particularly Charles Peguero, whose assistance has been invaluable. This work was supported by AFOSR (monitored by Drs Rhett Jeffries and Willard Larkin), NSF, and the Brown University UTRA program.

References

[1]Shkarayev, S., W. Null, and M. Wagner, *Development of Micro Air Vehicle Technology With In-Flight Adaptive-Wing Structure*, in *NASA Contractor Report*. 2004.

[2]Shyy, W., P. Ifju, and D. Viieru, *Membrane Wing-Based Micro Air Vehicles.* Applied Mechanics Reviews, 2005. **58**(2005): p. 283-301.

[3]Bishop, K.L., *The relationship between 3-D kinematics and gliding performance in the southern flying squirrel, Glaucomys volans.* Journal of Experimental Biology, 2006. **209**(4): p. 689-701.

[4]Norberg, U.M., *Vertebrate Flight: Mechanics, Physiology, Morphology, Ecology, and Evolution*. 1990, Berlin: Spring-Verlag.

[5]Dudley, R., *Mechanisms and implications of animal flight maneuverability.* American Zoologist, 2000. **40**(6): p. 1003-1003.

[6]Pennycuick, C.J., *Bird flight performance: a practical calculation manual*. Vol. 63. 1989, Oxford: Oxford University Press.***.

[7]Dudley, R., *The biomechanics of insect flight: form, function, evolution*. 2000, Princeton: Princeton University Press.
[8]Shyy, W., et al., *Rigid and Flexible Low Reynolds Number Airfoils.* Journal of Aircraft, 1999. **36**(3): p. 523-529.
[9]Torres, G.E. and T.J. Mueller, *Low-Aspect-Ratio Wing Aerodynamics at Low Reynolds Numbers.* AIAA Journal, 2004. **42**(5): p. 865-873.
[10]Pelletier, A. and T.J. Mueller, *Low Reynolds Number Aerodynamics of Low-Aspect-Ratio Thin/Flat/Cambered-Plate Wings.* AIAA Journal, 2000. **37**(5): p. 825-832.
[11]Swartz, S.M., K.L. Bishop, and M.-F. Ismael-Aguirre, *Dynamic complexity of wing form in bats: implications for flight performance*, in *Functional and evolutionary ecology of bats*, Z. Akbar, G. McCracken, and T.H. Kunz, Editors. 2005, Oxford University Press: Oxford.
[12]Mikhail, E., J. Bethel, and J. McGlone, *Introduction to Modern Photogrammetry*. 2001, New York: John Wiley & Sons, Inc.